Inverse Problems **26** (2010) 115003 (20pp) doi:10.1088/0266-5611/26/11/115003

Photoacoustic tomography in absorbing acoustic media using time reversal

Bradley E Treeby, Edward Z Zhang and B T Cox

Department of Medical Physics and Bioengineering, University College London, Gower Street, London WC1E 6BT, UK

E-mail: btreeby@mpb.ucl.ac.uk

Received 7 May 2010, in final form 20 August 2010
Published 24 September 2010
Online at stacks.iop.org/IP/26/115003

Abstract

The reconstruction of photoacoustic images typically neglects the effect of acoustic absorption on the measured time domain signals. Here, a method to compensate for acoustic absorption in photoacoustic tomography is described. The approach is based on time-reversal image reconstruction and an absorbing equation of state which separately accounts for acoustic absorption and dispersion following a frequency power law. Absorption compensation in the inverse problem is achieved by reversing the absorption proportionality coefficient in sign but leaving the equivalent dispersion parameter unchanged. The reconstruction is regularized by filtering the absorption and dispersion terms in the spatial frequency domain using a Tukey window. This maintains the correct frequency dependence of these parameters within the filter pass band. The method is valid in one, two and three dimensions, and for arbitrary power law absorption parameters. The approach is verified through several numerical experiments. The reconstruction of a carbon fibre phantom and the vasculature in the abdomen of a mouse are also presented. When absorption compensation is included, a general improvement in the image magnitude and resolution is seen, particularly for deeper features.

1. Introduction

1.1. Photoacoustic tomography and time-reversal image reconstruction

Photoacoustic tomography (PAT) is an emerging biomedical imaging modality that is particularly useful for visualizing light-absorbing structures embedded in soft tissue [1]. The technique works by externally illuminating the area to be imaged with short pulses of monochromatic laser light. Depending on the optical wavelength of the input pulse, photons are preferentially absorbed by endogeneous chromophores such as hemoglobin, melanin and water. The transfer of energy due to optical absorption causes a localized

increase in acoustic pressure via thermoelastic expansion. Due to the elastic nature of soft tissue, this pressure increase then propagates outwards as an acoustic wave. The acoustic waves arriving at the tissue surface are detected using an array of ultrasound transducers that partially or completely surround the tissue sample under investigation. Using the recorded pressure time signals, an image of the initial pressure distribution can then be reconstructed [2]. This reconstruction is equivalent to an inverse initial value problem in acoustics, or, in the homogeneous case, the recovery of a function from a set of its spherical means [3]. The modality has been demonstrated via high-resolution *in vivo* images of vasculature and cancer pathologies in small animals and humans over several length scales [4]. If the distribution of light within the tissue can be estimated, multiple photoacoustic images made using laser pulses with different optical wavelengths can be used to extract the concentration of the embedded chromophores [5]. Molecular imaging is also possible by using targeted exogeneous contrast agents [6]. Two additional techniques exploiting the thermoelastic generation of ultrasound analogous to PAT are also available. By using a focused laser source and ultrasound detector (a technique called photoacoustic microscopy), high resolution imaging of superficial absorbers can be performed without the need for tomographic reconstruction [7]. Images can also be formed using lower frequency electromagnetic waves such as microwaves (a technique often called thermoacoustic tomography), where water is the primary endogeneous chromophore [8].

The reconstruction of photoacoustic images in PAT requires a mapping from the time-varying pressure signals recorded on the tissue surface to the three-dimensional initial pressure distribution within the illuminated sample. A large number of tomographic reconstruction techniques are currently available [2]. These may be categorized in a number of ways, for example by their adhesion to mathematical rigour (exact, non-exact, ad hoc), their assumptions or restrictions (homogeneous acoustic properties, specific detector geometries, etc), or their algorithmic approach (filtered backprojection, Fourier expansion, time reversal, etc). Exact reconstruction algorithms for spherical detector geometries based on the inversion of the spherical Radon transform via filtered backprojection have recently been studied in detail [9–12]. While mathematically elegant, these algorithms tend to be computationally intensive which restricts their practical usage. Alternative algorithms based on the harmonic decomposition of the imaging problem have also been proposed [13]. For a planar detector geometry, this type of reconstruction can be computed efficiently using the fast Fourier transform (FFT) [14, 15]. This approach has also been applied to planar detector geometries in reverberant cavities [16] and cubic detector geometries [17]. Similar decompositions exist for other geometries, but do not offer the same computational advantages [18, 19]. Other ad hoc reconstruction techniques have also been proposed, for example the inversion of the linear Radon transform analogous to x-ray computed tomography [20], and the delay-and-sum analogous to conventional beamforming [21]. Note the different reconstruction techniques are not necessarily equivalent and are often based on differing assumptions (for example the shape of the observation surface or the region of support for the photoacoustic source [22]). Consequently, the response of the algorithms to different types of measurement noise and uncertainty will also vary.

As an alternative to the above, image reconstruction can also be achieved by running a numerical model of the forward problem backwards in time (herein referred to as 'time reversal'). This approach works by re-transmitting the measured acoustic pressure signals into the domain in time-reversed order. It was first proposed as an experimental technique for focusing ultrasound through scattering media [23, 24]. (A large body of literature has now evolved covering time reversal in this context [25].) The application of time reversal to PAT was first suggested by Finch *et al* [9] and Xu and Wang [26, 27] and has since been

studied by a number of authors [22, 28–30]. It has recently been described as the 'least restrictive' reconstruction algorithm for PAT [22]. It is applicable to heterogeneous acoustic media, arbitrary detection geometries, and is not susceptible to image artefacts if part of the photoacoustic source lies outside the detection surface. Despite this, time reversal has not been widely used for PAT. This may be due to the lack of a sufficiently fast numerical model of the forward problem which can be used to compute the time reversal *in silico*, particularly for 3D reconstructions. However, as faster forward models become available, it is likely that time reversal will become an increasingly practical tool for large-scale inversions.

1.2. Modelling acoustic absorption

Typically, the temporal length of the excitation laser pulse used for illumination is several orders of magnitude shorter than the time it takes for the generated acoustic waves to travel to the tissue surface (nanoseconds compared to microseconds). The distribution of chromophores is also often strongly compartmentalized. This creates step-like pressure discontinuities between the optically absorbing regions and causes the generated photoacoustic waves to be very broadband. For example, for each laser pulse, a superficial network of blood vessels may generate ultrasound waves containing frequencies from tens of kilohertz to tens of megahertz. To illustrate, the average amplitude spectrum of the time-varying pressure signals from an *in vivo* measurement of the vasculature in the human palm recorded using a broadband Fabry–Perot sensor as reported in [31] is shown in figure 1(a). Over these frequencies, acoustic absorption in biological tissue has been experimentally shown to follow a frequency power law of the form [32]

$$\alpha = \alpha_0 \omega^y. \tag{1}$$

Here α_0 is the absorption coefficient in nepers $(\text{rad/s})^{-y}\ \text{m}^{-1}$, ω is the angular frequency in rad s^{-1}, and y is the power law exponent. For most tissue types, the power law exponent is in the range 1–1.5 [32]. As the acoustic waves propagate, the frequency-dependent acoustic absorption will alter the frequency spectrum of the original pulse. Similarly, for a given measurement sensitivity, this absorption will limit the range of frequency components that can be detected at the tissue surface.

Given an impulsive acoustic point source with a pressure amplitude of p_{source} (defined at a distance d_{source} from the source) and a detector with a noise equivalent measurement pressure of p_{noise}, the maximum detectable frequency $f_{\max}$ in MHz after the source has propagated a distance d can be estimated by

$$f_{\max}(d) = \left(\frac{20 \log_{10}(p_{\text{source}} d_{\text{source}} / p_{\text{noise}} d)}{100 \alpha_{0,\text{dB}} d} \right)^{1/y}. \tag{2}$$

This is obtained by equating the total amount of absorption as a function of frequency with the detection bandwidth corrected for spherical spreading. Here, $\alpha_{0,\text{dB}}$ is the absorption coefficient in dB $\text{MHz}^{-y}\ \text{cm}^{-1}$, d and d_{source} are in m, and the initial frequency response is assumed to be broadband. For a plane wave source, the distance parameters within the $\log_{10}(\ldots)$ term are removed. The peak photoacoustic pressures generated *in vivo* are typically 10–20 kPa while the noise equivalent pressure of a high sensitivity ultrasound sensor is on the order of 0.2 kPa [33]. This gives a dynamic range on the order of 40 dB. Figure 1(b) shows the maximum detectable frequency for $p_{\text{source}} = 20$ kPa, $d_{\text{source}} = 0.5$ mm and $p_{\text{noise}} = 0.2$ kPa. The bold lines correspond to absorption parameters of $\alpha_0 = 0.75$ dB $\text{MHz}^{-y}\ \text{cm}^{-1}$ and $y = 1.5$ (breast tissue) and the light lines to $\alpha_0 = 0.6$ dB $\text{MHz}^{-y}\ \text{cm}^{-1}$ and $y = 1$ (fatty tissue) [32]. The values for both point (solid lines) and plane wave (dashed lines) sources are shown. Despite an

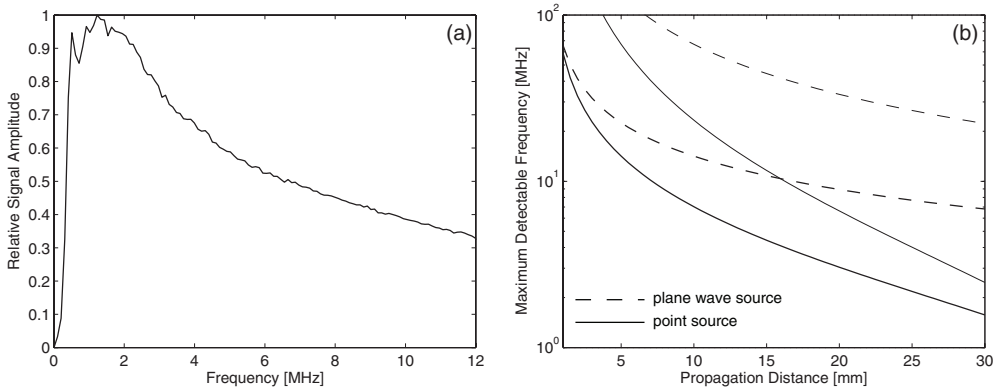

Figure 1. (a) The average frequency spectrum of the time-varying pressure recorded using a broadband ultrasound detector from an *in vivo* measurement of the vasculature in the human palm reported in [31]. (b) The maximum detectable frequency for an impulsive point source (solid lines) and plane wave source (dashed lines) in biological tissue with acoustic absorption parameters $\alpha_0 = 0.75$ dB MHz^{-y} cm^{-1} and $y = 1.5$ (bold lines) and $\alpha_0 = 0.6$ dB MHz^{-y} cm^{-1} and $y = 1$ (light lines).

initially broadband frequency response, after 20 mm the maximum frequency detectable from a point absorber is reduced to between 3 and 7 MHz (depending on the value of absorption used). This information loss is currently neglected in most photoacoustic image reconstruction methods and is the subject of interest here.

Notwithstanding the significant effect acoustic absorption can have on the measured frequency spectrum of photoacoustic waves in biological tissue, very few tomographic reconstruction methods for lossy media are available. This can in part be attributed to the lack of suitable acoustic forward models which can account for tissue realistic absorption. Classical lossy wave equations (such as Stokes' equation) which can include energy loss due to viscosity and thermal conduction yield an absorption that is proportional to frequency squared (i.e. $y = 2$) [34]. More recently, a number of other wave equations have been proposed that include phenomenological lossy operators based on convolution or the temporal fractional derivative (such as Szabo's equation [35]; see [36] for a recent review). While these equations can account for arbitrary power law absorption (and as such are suitable for modelling the absorption observed in biological tissue), they require the storage of the simulated pressure field at previous time steps and are thus very computationally expensive. To overcome these deficiencies, a wave equation with a lossy operator based on the fractional Laplacian can be used. This was first proposed in [37] and later extended to correctly account for power law dispersion [36]. Using this operator, no additional storage is needed as the value of the simulated pressure field at other positions (rather than times) is already inherently known. The corresponding equation of state can also be efficiently encoded using Fourier-based *k*-space or pseudospectral methods [38].

1.3. Image reconstruction in absorbing acoustic media

Within the limited literature on accounting for acoustic absorption in PAT, several different approaches have been suggested. Tan *et al* applied a correction to the frequency spectrum of the recorded signals before reconstruction [39]. This was achieved by applying a frequency

domain filter of the form $e^{\alpha(\omega)d}$ where the propagation distance d was assumed to be known and fixed. The absorption α was of the form given by (1) and the filter was regularized using the frequency response of the transducer. Experimental results showed a general deblurring effect after absorption correction. However, this approach is limited by the assumption of a constant propagation distance. Although correct when the photoacoustic signal is generated at this particular depth, for signals originating elsewhere, the spectrum will not be modified correctly. The filter is thus analogous to those used in conventional image sharpening. (Note a possible extension to this method might be to use a time-frequency representation to apply the filter with varying d).

La Rivière *et al* applied a more sophisticated absorption correction using Szabo's wave equation for $y = 1$ [40]. This correction was based on the computation of the pseudo-inverse of a discretized matrix equation relating the signals with and without acoustic absorption. The inversion was regularized by thresholding the matrix eigenvalues. Through numerical simulation, they showed a general de-blurring effect after their correction was applied. Burgholzer *et al* applied a 2D time-reversal reconstruction using a finite-difference implementation of Stokes' equation where $y = 2$ [41]. Regularization was reportedly performed using Fourier spectral methods. For numerical data simulated using the same equation, this approach also showed a general deblurring effect. Modgil *et al* derived an inversion formula for the initial photoacoustic pressure for $y = 1$ using singular value decomposition (SVD) [42]. Through this analysis, they showed that the smaller eigenvalues typically corresponded to deeper objects. These were, as intuitively expected, recovered less accurately. While useful as a numerical analysis tool, finding the SVD for experimental data sets of practical size becomes computationally intractable. Several other studies have also illustrated the effects of acoustic absorption in the forward problem [43–45]. However, a general and flexible method to account for acoustic absorption in photoacoustic tomography has not yet been reported.

Here, the absorption model discussed in [36] is combined with a time-reversed numerical model of ultrasound propagation to provide a flexible reconstruction algorithm for PAT in absorbing acoustic media. This represents a generalization of the method presented by Burgholzer *et al* [41]. The approach is valid in 1, 2 and 3D, for arbitrary detection geometries, and for arbitrary power law absorption parameters. The forward model is based on a k-space pseudospectral solution method to three coupled first-order acoustic equations. The forward and inverse problems for PAT in absorbing acoustic media are reviewed in section 2. The stability of the inverse problem when absorption correction is included is investigated using SVD. The regularization of the reconstruction by filtering the absorption terms is also discussed. In section 3, several numerical experiments are presented to illustrate the efficacy of the proposed reconstruction method. This is extended to experimental data in section 4. Both phantom and applied examples are provided. Summary and discussion are given in section 5.

2. Modelling photoacoustic waves in acoustically absorbing media

2.1. Forward and inverse acoustic propagation in photoacoustics

In a lossless acoustic medium, the photoacoustic wave equation can be reformulated as an initial value problem using three coupled acoustic equations. These are, respectively, the linearized equation of motion (conservation of momentum), the linearized equation of

continuity (conservation of mass) and the adiabatic equation of state [46]:

$$\frac{\partial}{\partial t}\mathbf{u}(\mathbf{x},t) = -\frac{1}{\rho_0(\mathbf{x})}\nabla p(\mathbf{x},t), \tag{3}$$

$$\frac{\partial}{\partial t}\rho(\mathbf{x},t) = -\rho_0(\mathbf{x})\nabla\cdot\mathbf{u}(\mathbf{x},t), \tag{4}$$

$$p(\mathbf{x},t) = c_0(\mathbf{x})^2\rho(\mathbf{x},t), \tag{5}$$

where the initial conditions are given by

$$p(\mathbf{x},t)|_{t=0} = p_0(\mathbf{x}), \qquad \mathbf{u}(\mathbf{x},t)|_{t=0} = 0. \tag{6}$$

Here, $p(\mathbf{x},t)$ is the acoustic pressure at time $t \in \mathbb{R}^+$ and position $\mathbf{x} \in \Omega \subset \mathbb{R}^n$ inside the imaging region Ω (n is typically 2 or 3), $\mathbf{u}(\mathbf{x},t)$ is the acoustic particle velocity, $c_0(\mathbf{x})$ is the sound speed, and $\rho(\mathbf{x},t)$ and $\rho_0(\mathbf{x})$ are the acoustic and ambient densities, respectively. In a lossy medium in which the acoustic absorption follows a general frequency power law in the form of (1), an alternative equation of state which contains two additional operators dependent on the fractional Laplacian is used to replace (5), where

$$p(\mathbf{x},t) = c_0(\mathbf{x})^2\left\{1 + \tau(\mathbf{x})\frac{\partial}{\partial t}(-\nabla^2)^{y/2-1} + \eta(\mathbf{x})(-\nabla^2)^{(y+1)/2-1}\right\}\rho(\mathbf{x},t). \tag{7}$$

The three bracketed terms correspond to the adiabatic equation of state, absorption and dispersion, respectively [36]. The latter causes a dependence of the sound speed on frequency. The absorption and dispersion proportionality coefficients, $\tau(\mathbf{x})$ and $\eta(\mathbf{x})$, are given by

$$\tau(\mathbf{x}) = -2\alpha_0 c_0(\mathbf{x})^{y-1}, \qquad \eta(\mathbf{x}) = 2\alpha_0 c_0(\mathbf{x})^y \tan(\pi y/2), \tag{8}$$

and α_0 and y are the absorption parameters from (1).

Given time-varying measurements $p_{\mathrm{m}}(\mathbf{x}_S,t)$ of the pressure $p(\mathbf{x}_S,t)$ recorded on an arbitrary measurement surface $\mathbf{x}_S \in S$ for some time $t = 0$ to T, the acoustic inverse problem in PAT is to reconstruct an estimate of the initial pressure distribution $p_0(\mathbf{x})$ inside the imaging region Ω. In time-reversal imaging, this reconstruction is achieved by enforcing $p_{\mathrm{m}}(\mathbf{x}_S,t)$ in time-reversed order as a Dirichlet boundary condition on $\hat{S} \subset \hat{\Omega}$ (here $\hat{S}$ and $\hat{\Omega}$ are the *in silico* equivalents of S and Ω). In this case, the initial pressure in (6) is set to zero, giving

$$p(\mathbf{x},t)|_{t=0} = 0, \qquad \mathbf{u}(\mathbf{x},t)|_{t=0} = 0, \qquad p(\mathbf{x}_S,t) = p_{\mathrm{m}}(\mathbf{x}_S, T-t), \tag{9}$$

where the pressure field in $\hat{\Omega}$ is computed for $t = 0$ to T. This is equivalent to the re-transmission of the pressure in a reflective cavity formed by $\hat{S}$ where $p_{\mathrm{m}}(\mathbf{x}_S, T-t)$ is injected as a source rather than imposed as a boundary condition [26].

To account for the acoustic absorption evident in the forward problem, the absorption term in (7) must be reversed in sign when computing the time-reversal reconstruction (the frequency content must grow according to (1) rather than decay). In contrast, to account for the dispersion evident in the forward problem, the frequency-dependent phase speed must remain unchanged (i.e., the dispersion term in (7) must not be reversed in sign). This is because, if higher frequencies have travelled to the detector faster than the lower frequencies, when the signal is reversed, they will again need to travel faster than the lower frequencies to correctly recover the original source shape (see figure 2). This is an important point that precludes the use of lossy wave equations in which the absorption and dispersion are encapsulated by a single term (such as Szabo's equation [35]). In this case, reversing the sign of the absorption coefficient would also incorrectly reverse the dispersion.

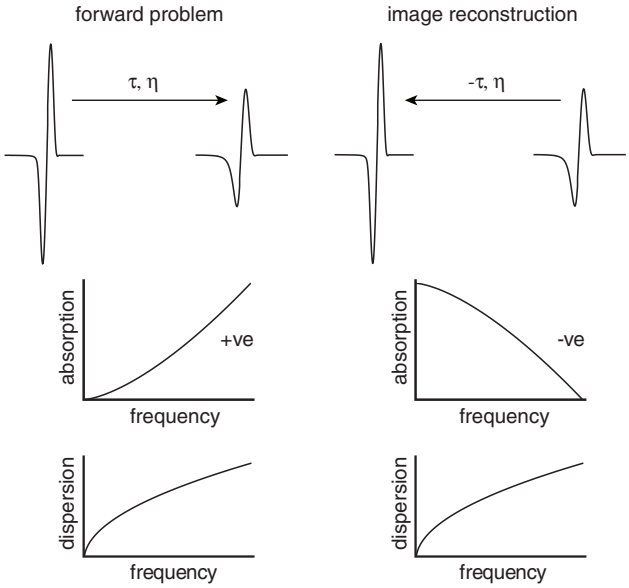

Figure 2. Time-reversal image reconstruction in absorbing acoustic media. To correctly account for absorption and dispersion, the absorption term must be reversed so it amplifies the signal as time progresses. In contrast, the dispersion term (dependence of the sound speed on frequency) must remain unchanged.

2.2. Artifact trapping

A consequence of the measured pressure field being enforced as a Dirichlet boundary condition within the imaging region $\hat{\Omega}$ during time reversal is that additional reconstruction artefacts can appear due to trapped vestigial waves [47]. This occurs when the acoustic properties of the propagation medium are heterogeneous, but only the average acoustic properties are known as input values for the reconstruction (this will most likely be the case in practice). In this case, the time-reversed waves do not interfere exactly to reproduce the outward going pressure field that resulted in the boundary measurements. As such, vestiges of the original reflections produced by the acoustic heterogeneities remain within the imaging region. When these waves reach the boundary $\hat{S}$, the enforced Dirichlet boundary condition causes these vestigial waves to be reflected back into the imaging region, ultimately resulting in additional image reconstruction artefacts (the problem of artifact trapping is discussed in detail in [47]). Here, to mitigate the effects of artifact trapping, a truncated data approach based on Huygens' principle is used. In 3D, for an acoustically homogeneous medium and a spherical measurement surface, no signals will be recorded after time $t_H = 2r/c_0$ (where r is the radius of the sensor surface). If c_0 is chosen to be the minimum sound speed in a heterogeneous medium, any signals arriving at the measurement surface after this time must arise from reflections from impedance interfaces (or otherwise are simply noise in the measurement data). The effects of artifact trapping can thus be reduced by truncating the measurement signals at t_H. Although Huygens' principle does not hold in 2D, the approach is still practically useful in this dimension for mitigating the effects of artefact trapping [47].

2.3. k-space methods

The most common method for solving partial differential equations in acoustics for broadband sources is the finite-difference time domain method [48]. In this approach, both spatial and

temporal derivatives are computed using finite differences. The accuracy of the solution is controlled by modifying the number of grid points per wavelength used to discretize the computational domain along with changing the length of the time steps. However, computational efficiency in the spatial domain can be significantly improved by using Fourier-based pseudospectral methods in which the spatial derivatives are calculated globally using the FFT [49]. This approach reduces the number of grid points per wavelength required to maintain a given level of accuracy (from ten points per wavelength for a second-order finite-difference to two points for a Fourier pseudospectral method). As the size of the time step is also related to the density of the grid points, this reduction can have a substantial effect on computational economy. The accuracy of the calculation of temporal derivatives can be further improved by using *k*-space pseudospectral methods [50]. In the homogeneous case, these models are exact for arbitrarily large time steps [51, 52]. In the case of heterogeneous media, the *k*-space adjustments lead to improved stability, and thus allow larger time steps for the same degree of accuracy [53]. For the range of heterogeneity evident in soft biological tissue, this increase is on the order of three to four times.

The coupled acoustic equations introduced in section 2.1 written in the discrete form using a *k*-space pseudospectral method are

$$\frac{\partial}{\partial \xi} p(\mathbf{x}, t) = \mathbb{F}^{-1}\{\mathrm{i} k_\xi \, \kappa \, \mathbb{F}\{p(\mathbf{x}, t)\}\}, \tag{10}$$

$$u_\xi(\mathbf{x}, t + \Delta t) = u_\xi(\mathbf{x}, t) - \frac{\Delta t}{\rho_0(\mathbf{x})} \frac{\partial}{\partial \xi} p(\mathbf{x}, t), \tag{11}$$

$$\frac{\partial}{\partial \xi} u_\xi(\mathbf{x}, t + \Delta t) = \mathbb{F}^{-1}\{\mathrm{i} k_\xi \, \kappa \, \mathbb{F}\{u_\xi(\mathbf{x}, t + \Delta t)\}\}, \tag{12}$$

$$\rho_\xi(\mathbf{x}, t + \Delta t) = \rho_\xi(\mathbf{x}, t) - \Delta t \rho_0(\mathbf{x}) \frac{\partial}{\partial \xi} u_\xi(\mathbf{x}, t + \Delta t), \tag{13}$$

$$p(\mathbf{x}, t + \Delta t) = c_0(\mathbf{x})^2 \left(\sum_\xi \rho_\xi(\mathbf{x}, t + \Delta t) + \mathrm{abs} + \mathrm{disp} \right). \tag{14}$$

Here, i is the imaginary unit, k_ξ is the spatial wavenumber component in the ξ direction where $k = \left(\sum_\xi k_\xi^2 \right)^{1/2}$, $\mathbb{F}\{\ldots\}$ and $\mathbb{F}^{-1}\{\ldots\}$ are the n-dimensional forward and inverse Fourier transforms, κ is the k-space adjustment to the spatial derivative where $\kappa = \mathrm{sinc}(c_0(\mathbf{x}) k \Delta t / 2)$ (this makes the finite-difference approximation of the temporal derivative exact in the homogeneous case [52]), Δt is the time step, and (10)–(13) are repeated for each Cartesian direction where $\xi = (x)$ in $\mathbb{R}^1$, $\xi = (x, y)$ in $\mathbb{R}^2$ and $\xi = (x, y, z)$ in $\mathbb{R}^3$. The density is artificially divided into Cartesian components to allow an anisotropic absorbing boundary layer to be applied [51]. Here, (10) and (12) are gradient calculations, (11) and (13) are update equations, and (14) is an equation of state which is explicitly included to allow absorption and dispersion to be incorporated in a transparent manner. The corresponding absorption and dispersion terms are given by

$$\mathrm{abs} = \tau(\mathbf{x}) \mathbb{F}^{-1} \left\{ (k \, \kappa)^{y-2} \mathbb{F} \left\{ \rho_0(\mathbf{x}) \sum_\xi \frac{\partial}{\partial \xi} u_\xi(\mathbf{x}, t + \Delta t) \right\} \right\},$$

$$\mathrm{disp} = \eta(\mathbf{x}) \mathbb{F}^{-1} \left\{ (k \, \kappa)^{y-1} \mathbb{F} \left\{ \sum_\xi \rho_\xi(\mathbf{x}, t + \Delta t) \right\} \right\}. \tag{15}$$

The equations are solved iteratively starting with the initial conditions for $p(\mathbf{x}, t)$, $u_\xi(\mathbf{x}, t)$ and $\rho_\xi(\mathbf{x}, t)$. For the forward problem in PAT, the initial conditions for the pressure and velocity are given by (6). If temporal staggered grids are used, the latter is enforced by setting $u(-\Delta t/2) = -u(\Delta t/2)$. The corresponding initial acoustic density distribution is calculated using (5), where the value for each Cartesian direction is chosen such that

$$\sum_\xi \rho_{0,\xi}(\mathbf{x}) = p_0(\mathbf{x})/c_0(\mathbf{x})^2, \tag{16}$$

where $\rho_\xi(\mathbf{x}, t)\big|_{t=0} = \rho_{0,\xi}(\mathbf{x})$. The time step Δt is chosen based on the Courant-Friedrichs-Lewy (CFL) number

$$\Delta t = \frac{\mathrm{CFL}\,\Delta x}{c_{\max}}, \tag{17}$$

where Δx is the size of the grid elements, and $c_{\max}$ is the maximum sound speed within the simulation medium. For the *k*-space model described here, a CFL number of 0.3 typically provides a good compromise between simulation accuracy and computational speed [51].

The *k*-space simulations and reconstructions presented here were computed using the *k*-Wave MATLAB toolbox [38]. This provides an implementation of (10)–(15) in one, two and three dimensions. The simulation functions within the toolbox also include an absorbing boundary layer to prevent waves leaving one side of the computational domain re-entering on the opposite side (in this case a perfectly matched layer or PML [51]). The computational grids are also spatially and temporally staggered to improve accuracy. Unless stated otherwise, the simulations are based on the acoustical properties of breast tissue in which the sound speed, density and absorption parameters are 1510 m s^{-1}, 1020 kg m^{-3}, $\alpha_0 = 0.75$ dB MHz^{-y} cm^{-1} and $y = 1.5$, respectively [32].

2.4. Singular value decomposition of the forward problem

To investigate the effect of acoustic absorption on the stability of the image reconstruction (inverse) problem, the discretized equations presented in the previous section may be rewritten using linear matrix operators which can then be analysed using SVD. In 1D, these become

$$u_+ = u_- - \mathrm{T}_1 p_-, \qquad \rho_+ = \rho_- - \mathrm{T}_2 u_+, \qquad p_+ = \mathrm{T}_3\rho_+ + \mathrm{T}_4 u_+. \tag{18}$$

Here the matrix operators are given by $\mathrm{T}_{1,2,\ldots}$ (these can be derived using (10)–(15) and the matrix form of the discrete Fourier transform), the subscript $_+$ and $_-$ symbols represent the solution at the next and previous time steps, respectively, and the function dependence has been omitted for clarity. Using these expressions and the initial conditions

$$p_- = p_0, \qquad u_- = 0, \qquad \rho_- = \mathrm{T}_5 p_0, \tag{19}$$

it is possible to derive a single matrix operator S_m to define the mapping of p_0 to p_m (the pressure field after m time steps). In this case $p_m = \mathrm{S}_m p_0$. For example, after one time step the pressure is given by $p_1 = \mathrm{S}_1 p_0$ where $\mathrm{S}_1 = \mathrm{T}_1\mathrm{T}_2\mathrm{T}_3 - \mathrm{T}_1\mathrm{T}_4 + \mathrm{T}_3\mathrm{T}_5$. The information loss due to acoustic absorption after m time steps can then be investigated by examining the singular values of the matrix operator S_m using SVD.

The singular values for S_1, S_5, S_{10} and S_{15} are shown in figure 3. These were computed using MATLAB's SVD function. The required matrix operators were calculated using a grid size of 512 pixels (10 mm in length supporting frequencies up to 38 MHz), a time step of 3 ns and the acoustic properties of breast tissue. The absorption coefficient was increased to $\alpha_0 = 50$ dB MHz^{-y} cm^{-1} to emulate the effect of taking a larger number of time steps (calculating S_m directly for $m \gg 1$ becomes intractable). For S_{15}, this is approximately

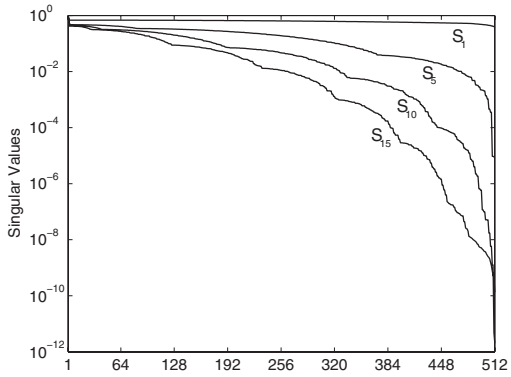

Figure 3. Singular values of the matrices S_1, S_5, S_{10} and S_{15} for absorption parameters $\alpha_0 = 50$ dB MHz^{-y} cm^{-1} and $y = 1.5$.

equivalent to taking 1000 time steps for $\alpha_0 = 0.75$ dB MHz^{-y} cm^{-1} with the wave propagating on the order of 5 mm. It is clear from figure 3 that as the number of time steps increases, some of the singular values of S_m become very small. Consequently, its inverse (an equivalent of which is required for image reconstruction accounting for acoustic absorption) will be poorly conditioned and the reconstruction will be very sensitive to noise in the measurement data. Numerically, if an image is reconstructed from real measurement data using time reversal based on (10)–(15) without regularization, noisy data at high frequencies (where the signal to noise ratio is typically much lower) will quickly grow to be larger than the signal data at lower frequencies, effectively masking the desired reconstruction of initial pressure.

2.5. Regularizing the absorption parameters

The inherent separation of the absorption and dispersion parameters from the adiabat (the $c_0^2\rho$ term) in (7) simplifies the task of regularizing the reconstruction. Here, this regularization is performed by filtering the abs and disp parameters in (15) in the spatial frequency domain before taking the inverse FFT. This prevents unwanted frequency content from growing in magnitude as the time-reversal reconstruction progresses. Assuming the smaller singular values correspond to higher spatial frequencies, this is similar to performing a truncated-SVD inversion. A frequency domain symmetric Tukey window (or tapered cosine window) scaled to a particular frequency cutoff was chosen as the filter shape so that the correct power law absorption and dispersion characteristics were maintained within the filter pass band. An example of the filter shapes in 1D for taper ratios of 0.5 and 0.25 and a cutoff frequency of 15 MHz are shown in figure 4(a). The analogous window in 2D for a taper ratio of 0.5 (constructed using rotation) is shown in 4(b).

The effect of the filter on the frequency-dependent absorption and dispersion experienced by a 1D monopolar plane wave pulse is shown in figures 4(c) and (d). A Tukey window with a cutoff frequency of 15 MHz and a taper ratio of 0.5 (solid lines) or 0.25 (dashed lines) was used to regularize the absorption parameters. The absorption and dispersion values were extracted from the time series recorded at 1 and 5 mm from the source [54]. The grid size was 2048 pixels (60 mm) supporting frequencies up to 25 MHz, and the medium parameters were based on breast tissue. Reference values from 0.1 to 20 MHz are also shown with open circles for comparison. These were calculated using (1) and the corresponding Kramers–

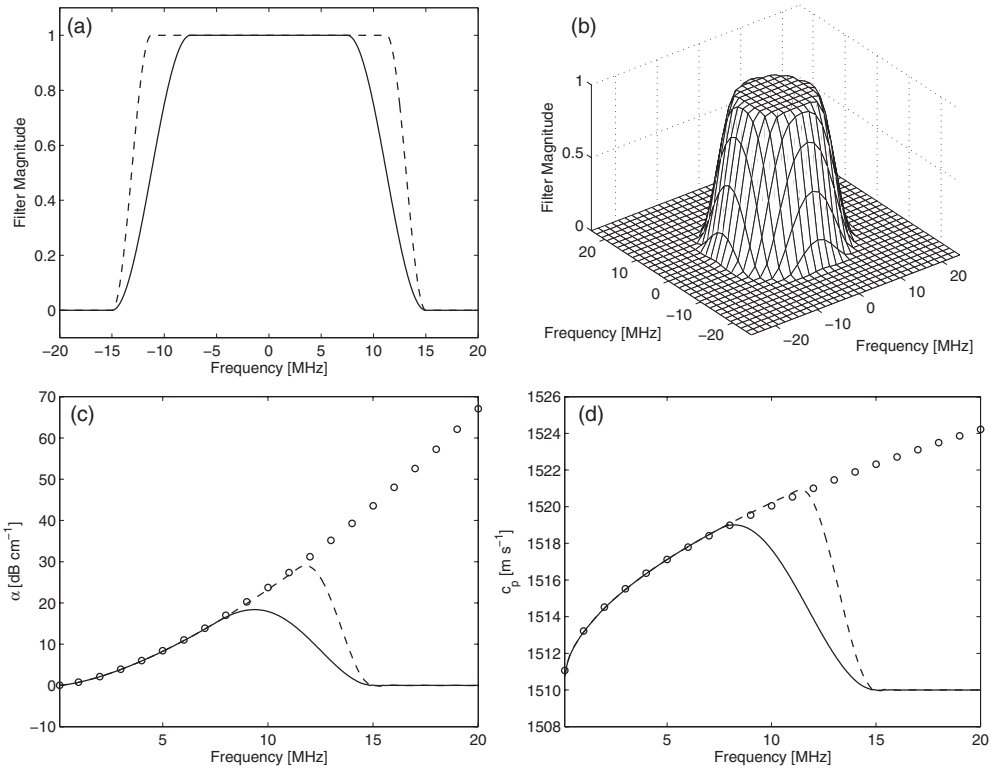

Figure 4. (a) One-dimensional symmetric Tukey window with a frequency cutoff of 15 MHz and taper ratios of 0.5 (solid line) and 0.25 (dashed line). (b) Two-dimensional symmetric Tukey window with a frequency cutoff of 15 MHz and a taper ratio of 0.5. (c) Effective acoustic absorption after filtering the absorption parameters with the Tukey windows shown in (a) for $\alpha_0 = 0.75$ dB MHz^{-y} cm^{-1} and $y = 1.5$. Reference values are shown as open circles for comparison. (d) Effective acoustic dispersion analogous to (c).

Kronig relations [55]. The reference frequency for the latter was chosen to be 5 MHz and the corresponding sound speed extracted from the simulated data. In the filter pass band, the absorption and dispersion correctly display the required frequency dependences. The parameters then smoothly change to be non-absorbing and non-dispersive in the filter stop band. For noisy data, a suitable filter cutoff frequency can be chosen by examining the power spectrum of the measured pressure signals and identifying a value based on where the observed signal spectrum reaches the noise floor.

3. Numerical simulations

3.1. Reconstruction of a point source

To demonstrate the effect of absorption compensation on images reconstructed using time reversal, the simulation and reconstruction of a point source in a 2D absorbing medium was investigated. A grid size of 476 × 476 pixels was used for the simulation (22 × 22 mm with an external 20 pixel PML), supporting frequencies up to 16 MHz. The medium parameters were again based on breast tissue. The initial pressure was set to be a single pixel positioned

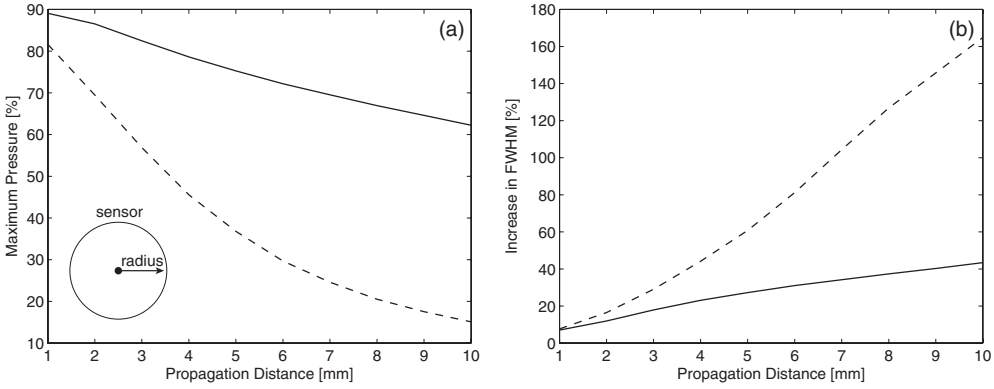

Figure 5. Reconstruction of a point source in an absorbing medium. The maximum and FWHM of the reconstruction are shown as a function of the propagation distance (sensor radius). The results from reconstructions both with (solid lines) and without (dashed lines) absorption compensation are shown.

in the centre of the grid and was smoothed using a frequency domain Hanning window. The pressure signals were recorded using a continuous circle of point detectors with a radius varying from 1 to 10 mm (see the inset in figure 5(a)). The signals were then time reversed using the same grid size with the absorption proportionality coefficient τ reversed in sign, and the absorption and dispersion operators filtered using a Tukey window with a taper ratio of 0.5 and a cutoff frequency of 16 MHz. The reconstruction was also performed with no absorption compensation. The maximum and the full width at half maximum (FWHM) of the reconstructed initial pressure were then extracted as a function of the propagation distance (i.e. the radius of the sensor). These are plotted in figure 5. The values for the absorption compensated reconstruction are shown as solid lines with the values without compensation shown as dashed lines for comparison. For this idealized example (using noiseless data and a complete measurement field of view), the absorption compensation significantly improves the reconstruction.

3.2. Shepp–Logan phantom

A second numerical example illustrating the effect of absorption compensation is shown in figure 6. Here the Shepp–Logan phantom [56] was used to define the initial photoacoustic pressure distribution using the phantom function in the MATLAB image processing toolbox (see figure 6(a)). The forward simulations were computed using a 984 $\times$ 984 pixel grid (52 $\times$ 52 mm with an external 20 pixel PML) which supported frequencies up to 14 MHz. The medium properties were based on breast tissue with the absorption coefficient increased to $\alpha_0 = 3$ dB MHz^{-y} cm^{-1} (based on human skin [57]). The signals were detected using a circle of 200 evenly distributed point detectors defined in Cartesian space with a radius of 25 mm. The pressure at the sensor points was calculated from the pressure at the grid points at each time step via linear interpolation. After the forward simulation, random Gaussian noise was added to the recorded signals to give a signal to noise ratio of 40 dB (based on the peak of the recorded signal and the rms noise level). The power spectrum of the signal recorded at the first sensor element is shown in figure 6(b). The average power spectrum of all the measurement signals is overlayed in bold. The time-reversal reconstructions were then computed using a different sized 974 $\times$ 974 pixel grid (with an external 25 pixel PML). Before reconstruction,

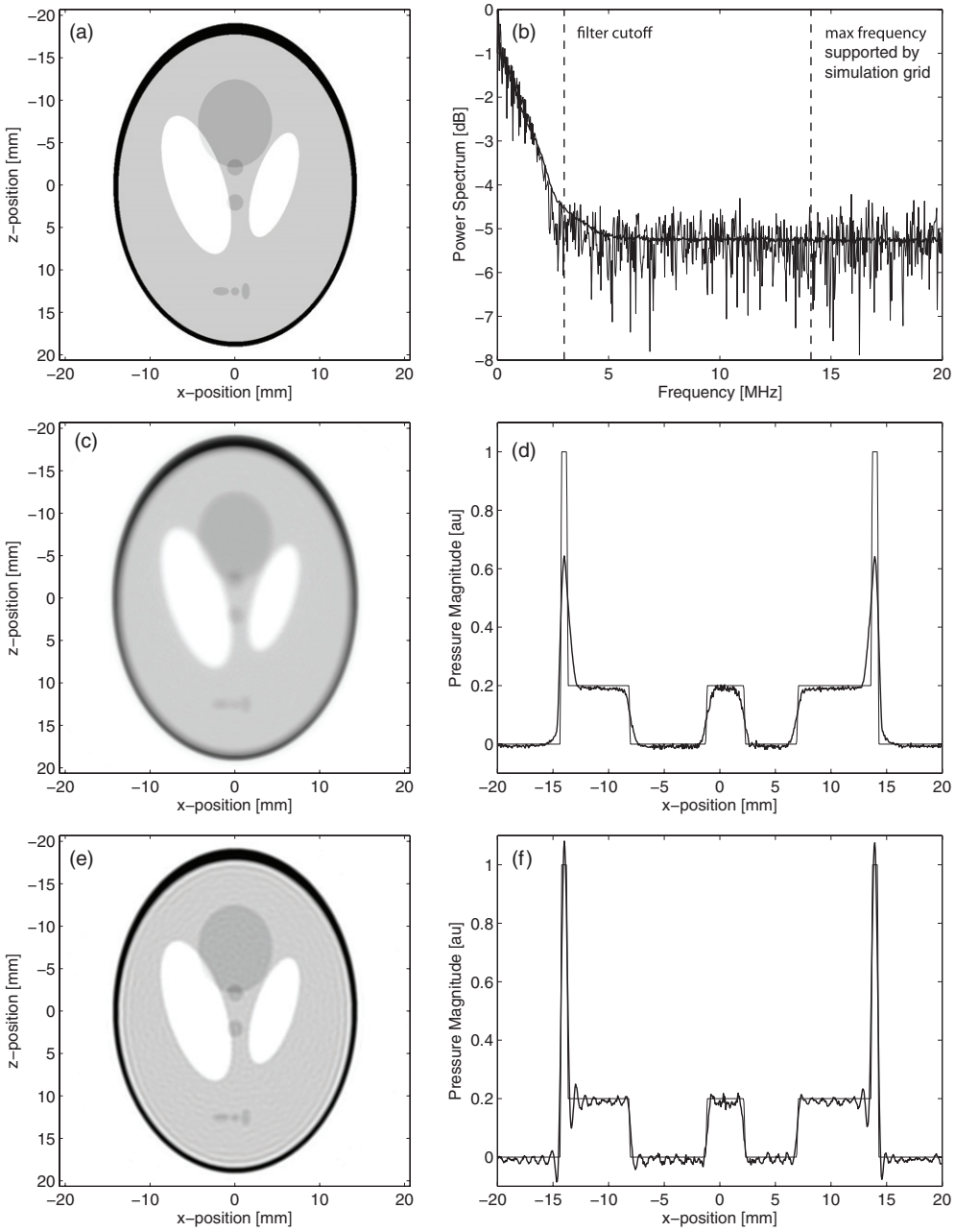

Figure 6. Time-reversal reconstruction of the Shepp–Logan phantom in absorbing acoustic media. (a) The initial acoustic pressure. (b) An example of the power spectrum of the measured signals. The average power spectrum of all the measured signals is overlayed in bold. (c) Time-reversal reconstruction with no compensation for acoustic absorption. (d) A profile through $z = 0$. The equivalent initial pressure is also shown for comparison. (e) Time-reversal reconstruction including compensation for acoustic absorption. (f) A profile through $z = 0$ analogous to (d).

the recorded signals were interpolated onto a continuous sensor surface with the same radius using linear interpolation [38]. These signals were then enforced as a time-varying Dirichlet boundary condition during the reconstruction. A Tukey window with a taper ratio of 0.5 and a cutoff frequency of 3 MHz was used to regularize the absorption parameters. The cutoff frequency was chosen based on the noise floor observable in figure 6(b).

The reconstructions both without and with absorption compensation are shown in figures 6(c) and (e), respectively. Profiles through $z = 0$ for both reconstructions are shown in figures 6(d) and (f) for comparison. Without correction for absorption, the edges of the reconstructed pressure become blurred, and the overall magnitude is reduced. When compensation for acoustic absorption is included into the reconstruction, the sharpness and magnitude of the reconstructed pressure is considerably improved. Due to the band-limited frequency response of the detected signals (high frequencies are not detected because their magnitudes are below the noise floor when the acoustic waves reach the sensor), the reconstruction is unable to completely recover the frequency content of the initial pressure distribution. This results in the Gibbs phenomenon appearing in the reconstruction where there are sharp changes in gradient.

4. Experimental measurements

4.1. Carbon fibre phantom

To illustrate the applicability of time reversal with absorption compensation (and the use of time reversal more generally) to experimental data, images from both phantom and *ex vivo* experiments were reconstructed. Figure 7 shows the 2D reconstruction of a 7 μm diameter carbon fibre phantom in distilled water. The fibre was illuminated with nanosecond laser pulses from a fiber coupled laser. The laser source used was a Q-switched Nd:YAG operating at 1064 nm with a pulse duration, energy and repetition frequency of 5.6 ns, 45 mJ and 20 Hz, respectively. A 7 mm line scan with a step size of 3 μm was taken perpendicular to the fibre axis using a photoacoustic scanner based on a Fabry–Perot interferometer [33]. Each waveform was acquired for 3 μs with a temporal resolution of 0.8 ns. The time-reversal reconstruction including absorption compensation is shown in figure 7(b) with a profile through $z = 0$ shown in figure 7(c). The reconstruction was performed using a 2048 $\times$ 1024 pixel grid supporting frequencies up to 215 MHz. The absorption parameters were set to $\alpha_0 = 2.17 \times 10^{-3}$ dB MHz^{-y} cm^{-1} and $y = 2$ [32]. A Tukey window with a taper ratio of 0.5 and a cutoff frequency of 200 MHz was used for regularization. A profile of the corresponding reconstruction without absorption compensation is also shown in figure 7(c) for comparison. The inclusion of absorption compensation increases the peak pressure by 17% and reduces the FWHM from 29.0 to 27.0 μm in the x-direction, and 14.7 to 13.9 μm in the z-direction (on the order of 6%). In this case the achievable resolution is also constrained by the limited measurement aperture and the frequency response of the detection system.

4.2. Ex vivo imaging of the vasculature in the mouse skin

Figure 8 shows the 3D time-reversal reconstruction of the vasculature in the skin around the abdomen of a mouse. The acquisition of the measurement data is reported in detail in [31]. The skin was illuminated by the output of a fibre coupled type I optical parametric oscillator pumped by the 355 nm frequency tripled output of a Q-switched Nd:YAG laser. The pulse duration, incident fluence, repetition rate and wavelength used were 8 ns, 6.8 mJ cm^{-2}, 10 Hz and 590 nm, respectively. A 10 mm area scan with a step size of 100 μm was performed,

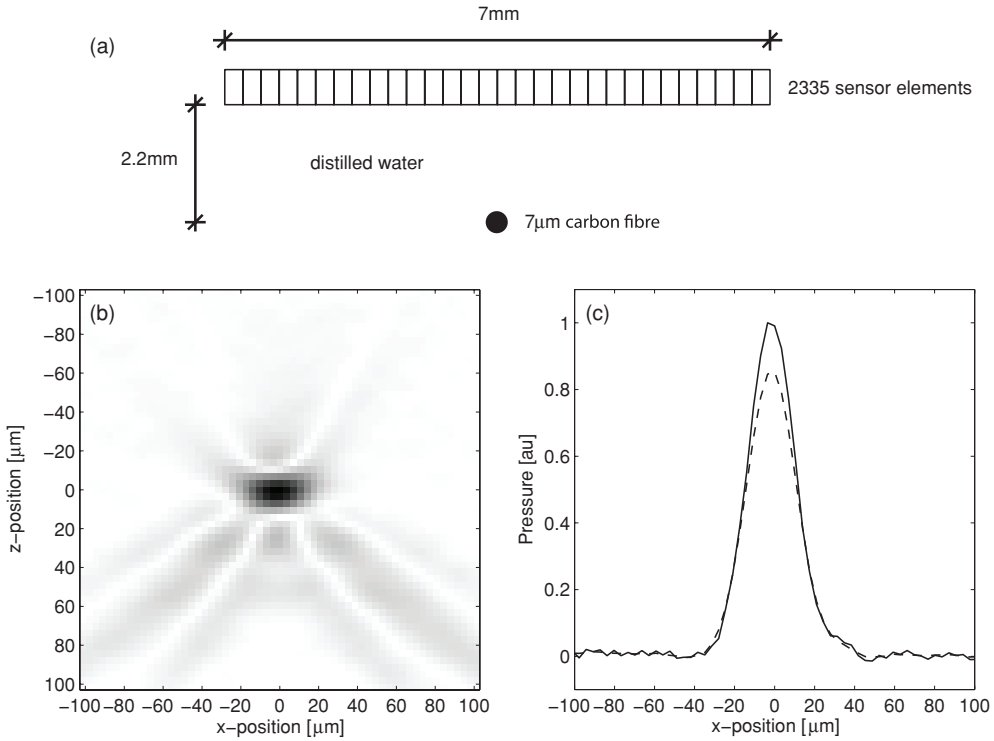

Figure 7. 2D reconstruction of a carbon fibre phantom in distilled water. (a) Schematic of the experimental setup. (b) Reconstructed fibre. (c) The x-profile through $z = 0$ both with (solid line) and without (dashed line) compensation for acoustic absorption.

with each waveform acquired for 2 μs with a temporal resolution of 8 ns. The measured pressure signals were interpolated using linear interpolation to give a twofold increase in lateral resolution before reconstruction. The time-reversal reconstruction was performed using a 200 $\times$ 200 $\times$ 295 pixel grid (10 $\times$ 10 $\times$ 3.6 mm with a 10 pixel external PML) which supported a maximum frequency of 15 MHz in the lateral direction and 62.5 MHz in the depth direction. The disparate grid size was chosen to match the resolution of the acquired data (the depth resolution is dependent on the temporal resolution of the acquisition system). A Tukey window with a taper ratio of 0.5 and a cutoff frequency set to 15 MHz in the lateral direction and 30 MHz in the depth direction was used to regularize the absorption parameters. The medium properties were set to breast tissue.

After reconstruction, a first-order correction for the optical attenuation in tissue was applied, where $p_0(\mathbf{x})_{\text{corrected}} = p_0(\mathbf{x})\, \mathrm{e}^{\mu_{\text{eff}} z}$. Here, z is the distance in the depth direction, and a value of $\mu_{\text{eff}} = 0.5\ \text{cm}^{-1}$ was used for the effective scattering coefficient. The resulting reconstructed initial pressure distributions with and without absorption compensation are shown in figure 8. The plots correspond to maximum intensity projections through the depth and lateral directions and an x-y slice at a depth of $z = 1.6$ mm. One-dimensional profiles through these images are also shown in figure 9 for comparison. When absorption compensation is included, the underlying vasculature becomes slightly more visible and the edges of the vessels become sharper. Although the images look qualitatively very similar, the peak pressure of the particular vessel profile shown in figure 9(b) is increased by 50%,

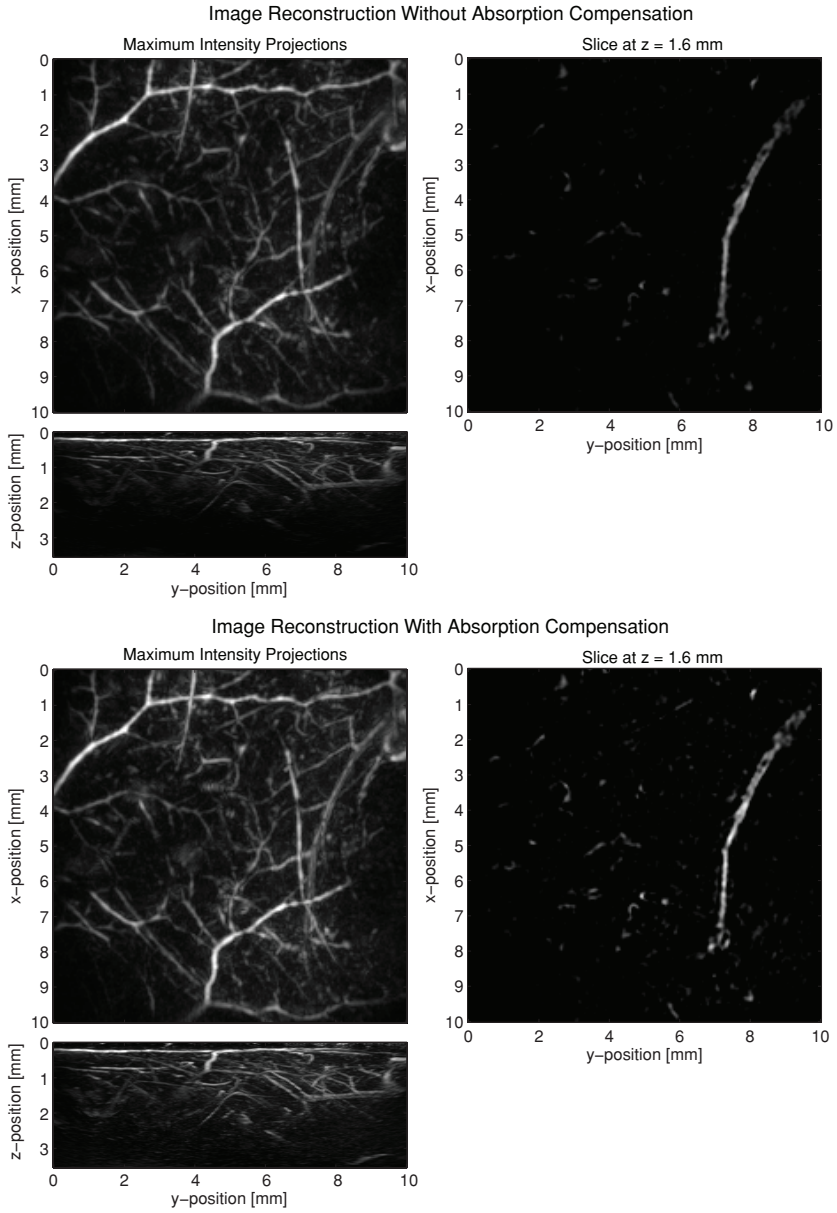

Figure 8. 3D time-reversal image reconstruction of the vasculature in the skin around the abdomen of a mouse. The upper plots show the reconstruction without compensation for acoustic absorption. The plots on the left show maximum intensity projections through the z (depth) and x (lateral) directions. An x–y slice at a depth of $z = 1.6$ mm is shown on the right. The lower plots show the analogous information when absorption compensation is included. The magnitude and sharpness of the deeper vessels are improved.

and the FWHM is reduced by 10%. In the context of quantitative imaging where absolute pressure values are required, variations of this order could significantly alter estimates of the underlying chromophore concentrations.

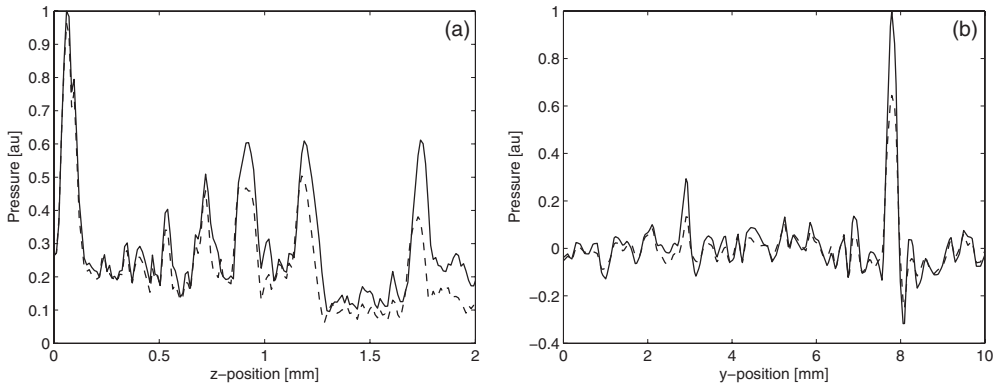

Figure 9. (a) 1D profile through the lateral maximum intensity projections shown in figure 8 for $y = 6.7$ mm. The magnitude of the three deeper vessels when compensation for acoustic absorption is included appears almost equal. (b) 1D profile through the x-y slices shown in figure 8 for $x = 4$ mm. The peak pressure of the main vessel is increased by 50%, and the FWHM is reduced by 10%. The solid and dashed lines in both plots correspond to the reconstructions with and without compensation for acoustic absorption, respectively.

5. Summary and discussion

A new method to compensate for acoustic absorption and dispersion in the reconstruction of images in photoacoustic tomography is described. The method is based on the idea of time-reversal image reconstruction in which a numerical model of the forward problem is run backwards in time. Here, a forward model which utilizes an absorbing equation of state based on the fractional Laplacian is used. This model contains terms which separately account for the acoustic absorption and dispersion evident in biological tissue. Absorption compensation in the inverse problem is achieved by reversing the absorption proportionality coefficient in sign but leaving the dispersion term unchanged. This is not possible when the absorption and dispersion are encapsulated by a single operator. The reconstruction is regularized by filtering the absorption and dispersion terms in the spatial frequency domain. A Tukey window is used to maintain the correct frequency dependence of these parameters in the filter pass band. The approach is demonstrated through the reconstruction of numerical and experimental data in both 2D and 3D. After reconstruction, a general improvement in image magnitude and resolution is seen, particularly for features at lower depths.

The practical application of the proposed absorption compensation technique raises several interesting questions. First, a method is required to select the properties of the filter used to regularize the absorption and dispersion parameters. Here, a filter cutoff frequency was chosen based on visual inspection of the average power spectrum of the recorded data. The cutoff was chosen at the frequency where the signal spectrum reached the noise floor. This selection (which is equivalent to selecting a regularization parameter) represents a compromise between correctly accounting for acoustic absorption and the desired reconstruction becoming masked by amplified high frequency noise. The exact balance between obtaining an image with adequate signal to noise and improving the accuracy of the reconstruction is dependent on the intended application. For example, if extracting quantitative information, the accuracy of the reconstructed initial pressure within regions of interest (e.g. within the vasculature) will likely take precedence. In this case, the accurate compensation of acoustic absorption is of particular importance, as errors in the magnitude of the reconstruction will manifest as errors

in the estimation of chromophore concentrations. Alternatively, if the images are simply for qualitative analysis or display, a reconstruction that yields a better overall signal to noise ratio may be preferable.

Second, for the compensation to be accurate, tissue realistic parameters for the acoustic absorption must be used in the reconstruction. While values for the absorption coefficient and power law exponent for several tissue types are readily available (e.g. [32]), the majority of these reference measurements have been taken over a limited frequency range (typically below 10 MHz). The validity of these values over a wider frequency range applicable to photoacoustics is not inherently assured. Additionally, the properties of many tissue types (for example human skin, or the tissues in mouse or other small animal models) have not been studied in detail. Further characterization of the relevant tissue parameters is thus required. If accurate maps of the tissue properties can be obtained (for example from a complementary imaging modality), it may be possible to assign segmented maps of acoustic absorption. This would provide a more realistic compensation for the absorption observed in the forward problem.

Finally, it is important to note that the achievable resolution of the reconstructed image will be limited by the properties of the photoacoustic scanning system used to take the measurements. If the features in the reconstructed image in a particular dimension are only one pixel in width, adding absorption compensation will have no effect on the resolution (although the magnitude of deeper structures may still be improved). Similarly, if the measurement system is bandlimited such that higher frequencies are not recorded, the effect of absorption correction on resolution will also be limited. However, given sufficiently high resolution measurement data and a realistic characterization of the absorption parameters, the proposed technique can accurately compensate for the effects of acoustic absorption in photoacoustic tomography.

Acknowledgments

This work was supported by the Engineering and Physical Sciences Research Council, UK.

References

[1] Wang L V (ed) 2009 *Photoacoustic Imaging and Spectroscopy* (Boca Raton, FL: CRC Press)
[2] Kuchment P and Kunyansky L 2008 Mathematics of thermoacoustic tomography *Eur. J. Appl. Math.* **19** 191–224
[3] Xu M and Wang L V 2002 Time-domain reconstruction for thermoacoustic tomography in a spherical geometry *IEEE Trans. Med. Imaging* **21** 814–22
[4] Wang L V 2009 Multiscale photoacoustic microscopy and computed tomography *Nat. Photon.* **3** 503–9
[5] Laufer J, Cox B, Zhang E and Beard P 2010 Quantitative determination of chromophore concentrations from 2D photoacoustic images using a nonlinear model-based inversion scheme *Appl. Opt.* **49** 1–15
[6] de la Zerda A, Zavaleta C, Keren S, Vaithilingam S, Bodapati S, Liu Z, Levi J, Smith B R, Ma T J and Oralkan O 2008 Carbon nanotubes as photoacoustic molecular imaging agents in living mice *Nat. Nanotechnol.* **3** 557–62
[7] Zhang H F, Maslov K, Stoica G and Wang L V 2006 Functional photoacoustic microscopy for high-resolution and noninvasive in vivo imaging *Nat. Biotechnol.* **24** 848–51
[8] Wang L V 2009 Microwave-induced acoustic (thermoacoustic) tomography *Photoacoustic Imaging and Spectroscopy* ed ed L V Wang (Boca Raton, FL: CRC Press) pp 339–47
[9] Finch D, Patch S K and Rakesh 2004 Determining a function from its mean values over a family of spheres *SIAM J. Math. Anal.* **35** 1213–40
[10] Xu M and Wang L V 2005 Universal back-projection algorithm for photoacoustic computed tomography *Phys. Rev.* E **71** 016706

[11] Finch D, Haltmeier M and Rakesh 2007 Inversion of spherical means and the wave equation in even dimensions *SIAM J. Appl. Math.* **68** 392–412
[12] Kunyansky L A 2007 Explicit inversion formulae for the spherical mean Radon transform *Inverse Problems* **23** 373–83
[13] Norton S J and Linzer M 1981 Ultrasonic reflectivity imaging in three dimensions: exact inverse scattering solutions for plane, cylindrical, and spherical apertures *IEEE Trans. Biomed. Eng.* **28** 202–20
[14] Fawcett J 1985 Inversion of *n*-dimensional spherical averages *SIAM J. Appl. Math.* **45** 336–41
[15] Köstli K P, Frenz M, Bebie H and Weber H P 2001 Temporal backward projection of optoacoustic pressure transients using Fourier transform methods *Phys. Med. Biol.* **46** 1863–72
[16] Cox B T, Arridge S R and Beard P C 2007 Photoacoustic tomography with a limited-aperture planar sensor and a reverberant cavity *Inverse Problems* **23** S95–112
[17] Kunyansky L A 2007 A series solution and a fast algorithm for the inversion of the spherical mean Radon transform *Inverse Problems* **23** S11–20
[18] Xu Y, Xu M and Wang L V 2002 Exact frequency-domain reconstruction for thermoacoustic tomography: II. Cylindrical geometry *IEEE Trans. Med. Imaging* **21** 829–33
[19] Anastasio M A, Zhang J, Modgil D and La Rivière P J 2007 Application of inverse source concepts to photoacoustic tomography *Inverse Problems* **23** S21–35
[20] Kruger R A, Liu P, Fang Y R and Appledorn C R 1995 Photoacoustic ultrasound (PAUS)—Reconstruction tomography *Med. Phys.* **22** 1605–9
[21] Hoelen C G A and de Mul F F M 2000 Image reconstruction for photoacoustic scanning of tissue structures *Appl. Opt.* **39** 5872–83
[22] Hristova Y, Kuchment P and Nguyen L V 2008 Reconstruction and time reversal in thermoacoustic tomography in acoustically homogeneous and inhomogeneous media *Inverse Problems* **24** 055006
[23] Jackson D R and Dowling D R 1991 Phase conjugation in underwater acoustics *J. Acoust. Soc. Am.* **89** 171–81
[24] Fink M 1992 Time reversal of ultrasonic fields: part I. Basic principles *IEEE Trans. Ultrason. Ferroelectr. Freq. Control* **39** 555–66
[25] Fink M and Prada C 2001 Acoustic time-reversal mirrors *Inverse Problems* **17** R1–38
[26] Xu Y and Wang L V 2004 Time reversal and its application to tomography with diffracting sources *Phys. Rev. Lett.* **92** 033902
[27] Xu Y and Wang L V 2004 Application of time reversal to thermoacoustic tomography *Proc. SPIE* **5320** 257–63
[28] Burgholzer P, Matt G J, Haltmeier M and Paltauf G 2007 Exact and approximative imaging methods for photoacoustic tomography using an arbitrary detection surface *Phys. Rev.* E **75** 046706
[29] Grün H, Nuster R, Paltauf G, Haltmeier M and Burgholzer P 2008 Photoacoustic tomography of heterogeneous media using a model-based time reversal method *Proc. SPIE* **6856** 685620
[30] Hristova Y 2009 Time reversal in thermoacoustic tomography—an error estimate *Inverse Problems* **25** 055008
[31] Zhang E Z, Laufer J G, Pedley R B and Beard P C 2009 In vivo high-resolution 3D photoacoustic imaging of superficial vascular anatomy *Phys. Med. Biol.* **54** 1035–46
[32] Szabo T L 2004 *Diagnostic Ultrasound Imaging* (London: Elsevier)
[33] Zhang E Z, Laufer J G and Beard P C 2008 Backward-mode multiwavelength photoacoustic scanner using a planar Fabry–Perot polymer film ultrasound sensor for high-resolution three-dimensional imaging of biological tissues *Appl. Opt.* **47** 561–77
[34] Markham J J, Beyer R T and Lindsay R B 1951 Absorption of sound in fluids *Rev. Mod. Phys.* **23** 353–411
[35] Szabo T L 1994 Time domain wave equations for lossy media obeying a frequency power law *J. Acoust. Soc. Am.* **96** 491–500
[36] Treeby B E and Cox B T 2010 Modeling power law absorption and dispersion for acoustic propagation using the fractional Laplacian *J. Acoust. Soc. Am.* **127** 2741–8
[37] Chen W and Holm S 2004 Fractional Laplacian time-space models for linear and nonlinear lossy media exhibiting arbitrary frequency power-law dependency *J. Acoust. Soc. Am.* **115** 1424–30
[38] Treeby B E and Cox B T 2010 k-Wave: MATLAB toolbox for the simulation and reconstruction of photoacoustic wave-fields *J. Biomed. Opt.* **15** 021314
[39] Tan Y, Da Xing Y W and Yang D 2005 Photoacoustic imaging with attenuation rectification of different frequent components of photoacoustic signal *Proc. SPIE* **5630** 668–74
[40] La Rivière P J, Zhang J and Anastasio M A 2006 Image reconstruction in optoacoustic tomography for dispersive acoustic media *Opt. Lett.* **31** 781–3
[41] Burgholzer P, Grün H, Haltmeier M, Nuster R and Paltauf G 2007 Compensation of acoustic attenuation for high-resolution photoacoustic imaging with line detectors *Proc. SPIE* **6437** 643724
[42] Modgil D and La Rivière P J 2008 Photoacoustic image reconstruction in an attenuating medium using singular-value decomposition *IEEE Nuclear Science Symposium Conf. Record, 2008* pp 4489–93

[43] Patch S K and Haltmeier M 2006 Thermoacoustic tomography—ultrasound attenuation artifacts *IEEE Nuclear Science Symposium Conf. Record, 2006* pp 2604–6
[44] Esenaliev R O, Alma H, Tittel F K and Oraevsky A A 1998 Axial resolution of laser opto-acoustic imaging: influence of acoustic attenuation and diffraction *Proc. SPIE* **3254** 294–306
[45] Treeby B E and Cox B T 2009 Fast, tissue-realistic models of photoacoustic wave propagation for homogeneous attenuating media *Proc. SPIE* **7716** 717716
[46] Cox B T and Beard P C 2009 Modeling photoacoustic propagation in tissue using *k*-space techniques *Photoacoustic Imaging and Spectroscopy* ed L V Wang (Boca Raton, FL: CRC Press) pp 25–34
[47] Cox B T and Treeby B E 2010 Artifact trapping during time reversal photoacoustic imaging for acoustically heterogeneous media *IEEE Trans. Med. Imaging* **29** 387–96
[48] Alford R M, Kelly K R and Boore D M 1974 Accuracy of the finite-difference modeling of the acoustic wave equation *Geophysics* **39** 834–42
[49] Fornberg B 1996 *A Practical Guide to Pseudospectral Methods* (Cambridge: Cambridge University Press)
[50] Bojarski N N 1982 The *k*-space formulation of the scattering problem in the time domain *J. Acoust. Soc. Am.* **72** 570–84
[51] Tabei M, Mast T D and Waag R C 2002 A *k*-space method for coupled first-order acoustic propagation equations *J. Acoust. Soc. Am.* **111** 53–63
[52] Cox B T, Kara S, Arridge S R and Beard P C 2007 *k*-space propagation models for acoustically heterogeneous media: application to biomedical photoacoustics *J. Acoust. Soc. Am.* **121** 3453–64
[53] Mast T D, Souriau L P, Liu D L D, Tabei M, Nachman A I and Waag R C 2001 A *k*-space method for large-scale models of wave propagation in tissue *IEEE Trans. Ultrason. Ferroelectr. Freq. Control* **48** 341–54
[54] Treeby B E, Cox B T, Zhang E Z, Patch S K and Beard P C 2009 Measurement of broadband temperature-dependent ultrasonic attenuation and dispersion using photoacoustics *IEEE Trans. Ultrason. Ferroelectr. Freq. Control* **56** 1666–76
[55] Waters K R, Hughes M S, Mobley J, Brandenburger G H and Miller J G 2000 On the applicability of Kramers–Kronig relations for ultrasonic attenuation obeying a frequency power law *J. Acoust. Soc. Am.* **108** 556–63
[56] Shepp L and Logan B 1974 Reconstructing interior head tissue from X-ray transmissions *IEEE Trans. Nucl. Sci.* **21** 228–36
[57] Guittet C, Ossant F, Vaillant L and Berson M 1999 In vivo high-frequency ultrasonic characterization of human dermis *IEEE Trans. Biomed. Eng.* **46** 740–6